Ultrathin RuRh@(RuRh)O_2 core@shell nanosheets as stable oxygen evolution electrocatalysts

Kai Wang,[1,†] Bolong Huang,[2,†] Weiyu Zhang,[1] Fan Lv,[1] Yi Xing,[1] Wenshu Zhang,[1] Jinhui Zhou,[1] Wenxiu Yang,[1] Peng Zhou,[1] Mingqiang Li,[3] Peng Gao[3] and Shaojun Guo[1,4]*

[1]Department of Materials Science and Engineering, College of Engineering, Peking University, Beijing 100871, China.

[2]Department of Applied Biology and Chemical Technology, The Hong Kong Polytechnic University, Hung Hom, Kowloon, Hong Kong SAR, 999077 China.

[3]Electron Microscopy Laboratory, and International Center for Quantum Materials School of Physics Peking University, Beijing 100871, China.

[4]BIC-ESAT, College of Engineering, Peking University, Beijing 100871, China.

[†] These authors contributed equally to this work.

*Correspondence: guosj@pku.edu.cn

Abstract

The oxygen evolution reaction (OER) is of prime importance in the development of highly efficient electrochemical energy conversion and storage technologies such as water splitting and zinc air battery. Ru-based nanocatalysts are still the best catalytic system for OER, however, one of their greatest challenges for OER is their relatively poor stability. Here, we report a novel architecture of ultrathin RuRh@(RuRh)O_2 core/shell nanosheets with core of ultrathin metallic RuRh nanosheets and shell of RuO_2/RhO_2 oxides as superb electrocatalysts toward OER. The RuRh@(RuRh)O_2 core/shell nanosheets can achieve the high electrocatalytic activity toward OER, with a low 245 mV overpotential at 10 mA cm^{-2} and a Tafel slope of 51.2 mV dec^{-1}. Moreover, the RuO_2/RhO_2 oxides shell protects the normally labile RuRh NS core against dissolution during OER process, revealed by detailed rotating ring disk electrode (RRDE) measurements for simultaneous recording the dissolution of Ru on the ring electrode or the ex-situ measurement of Ru dissolution using the galvanostatic method. Therefore, the RuRh@(RuRh)O_2 core/shell nanosheets exhibt much better OER stability in acid media compared with the RuRh nanosheets and commercial RuO_2. Theoretical calculations reveal that once the formation of the surface oxidation layers, the O-sites evidentially crossover the Fermi level could guarantee the high electroactivity towards adsorbates while the RuRh core

serves as an electron reservoir with high electrical conductivity. The synergistic effect between the core and shell structure leads to the superior OER performance.

Keywords: heterogeneous catalysts, 2D nanosheets, core-shell structure, oxygen evolution reaction

Introduction

Electrocatalytic splitting of water into molecular hydrogen and oxygen using polymer electrolyte membrane (PEM) electrolyzer architectures plays a critical role in the conversion of renewable electrical energy into fuels.[1] The splitting of water involves two related electrochemical reactions in an electrolyzer, with an anodic oxygen evolution reaction (OER) and a cathodic hydrogen evolution reaction (HER). Compared with the two-electron HER proceeding at the cathode, the anodic OER is the bottleneck in this process due to the sluggish kinetics of multiple-proton-coupled electron transfer under high oxidative potential, and hence dominates the large overpotential of the whole overall water electrolysis devices.[2] Therefore, the search for OER electrocatalysts with high intrinsic activity and preferable stability, especially in acid media, remains an outstanding problem so far.[2c, 3] Ruthenium and its oxides have been proved to be the most active oxygen evolution reaction (OER) catalysts.[4] However, despite its highest activity,[4-5] metallic Ru would deactivate very fastly during OER due to the fast dissolution of oxidized Ru species,[6] and the dissolution rate of Ru is 2-3 orders of magnitude higher than that of its respective oxides.[7] Therefore, it is of significant importance to design Ru-based nanostructures that enhance the stability without sacrificing their high activity,[8] however, achieving such target is still a grand challenge.

Herein, we propose a method to design an ultrathin RuRh@(RuRh)O_2 core/shell nanosheet consisting of ultrathin metallic RuRh nanosheets as core and few layers of RuO_2/RhO_2 oxides as shell. The RuRh@(RuRh)O_2 core/shell nanosheets have superb electrocatalytic activity toward OER, with a low 245 mV overpotential at 10 mA $cm^{-2}$and a Tafel slope of 51.2 mV dec^{-1}. Besides, ultrathin RuRh@(RuRh)O_2 core/shell nanosheets exhibt much better OER stability and Faradaic efficiency than RuRh NS because the covering layer of RuO_2/RhO_2 oxides shell can prevent the fast Ru dissolution of metallic RuRh NS core during OER, which is certificated by the RRDE measurements for simultaneous recording the dissolution of Ru on the ring electrode and the ex-situ measurement of Ru dissolution using the galvanostatic method. DFT systematically investigates the electronic modulations induced by the oxidation surface to the electroactivity of the core@shell RuRh@(RuRh)O_2. Both electronic and

energetic calculations indicate the boosting up effect on OER performance originates from the highly electroactive oxidation layer, supporting the experimental observations.

Ultrathin RuRh@(RuRh)O_2 core/shell nanosheets were synthesized *via* a two-step methods. Firstly, ultrathin RuRh nanosheets (RuRh NS) were synthesized by a colloidal-chemical approach. Then, the ultrathin RuRh nanosheets were loaded on carbon black (denoted as RuRh NS/C) and annealed in air at 286 °C for 2 h to obtain the ultrathin RuRh@(RuRh)O_2 core@shell nanosheets supported on carbon (denoted as RuRh@(RuRh)O_2 NS/C). Transmission electron microscopy (TEM) and high-resolution transmission electron microscopy (HRTEM) were conducted to investigate the morphology and structure of the as-obtained products. As shown in **Figure 1a&1b,** triangle nanosheets with the edge length of 16.3 ± 3.5 nm and the thickness of 1.9 ± 0.5 nm (six to eight atomic layers, **Figure S1**) were the dominant products. The Ru/Rh composition was 85/15 (Ru/Rh), determined by the TEM energy-dispersive X-ray spectroscopy (TEM-EDX) results (**Figure S2**). The Powder X-ray diffraction (PXRD) pattern of the RuRh nanosheets shows that they are highly crystalline with the hexagonal close-packed (*hcp*) phase of Ru (P63/mmc) crystals [JCPDS 06-0663] (**Figure S3**).[9] HRTEM and selected-area electron diffraction (SAED) image (**Figure 1c**) indicate that the triangle nanosheets are single-crystalline, with regular hcp structure that extends along the *c*-axis.

After being annealed in air at the phase transition temperature of 286 °C (**Figure S4**) for 2 h, the RuRh NS/C (**Figure S5)** still maintain the 2D morphology (**Figure S6**). PXRD result reveals that diffraction peaks of tetragonal RuO_2 (P42/mnm) crystals [JCPDS 40-1290][10] and tetragonal RhO_2 (P42/mnm) crystals [JCPDS 43-1026][11] appear (**Figure 1d**). The HAADF-STEM image (**Figure 1e** and **Figure S7**) shows that the annealed RuRh NS is transformed to a core/shell structure, with RuRh NS inside as core and the RuO_2/RhO_2 outside as shell. X-ray photoelectron spectroscopy (XPS) was used to study the chemical states of Ru and Rh after after the annealing process, and all the binding energies were calibrated to C 1s carbon at 284.8 eV (**Figure S8**) to eliminate differences in sample charging.[12] As shown in **Figure 1e**, the XPS of the RuRh@(RuRh)O_2 NS in the Ru 3p region and Rh 3d region show obvious positive shift of 0.3-0.4 eV compared with those of the RuRh NS, indicating the RuRh@(RuRh)O_2 NS exhibits higher valence state of oxized species than the RuRh NS due to the surface oxidation of thremal annealing.[13] The elemental distribution of the core@shell structure was characterized by aberration-corrected STEM-EDX (**Figure 1g**), showing that Ru and Rh distribute uniformly in the

RuRh@(RuRh)O_2 NS while the oxygen signals are more abundant in the shell compared with that of the core, further verifying the formation of the core@shell structure after the annealing process.

The OER activity of the RuRh NS, RuRh@(RuRh)O_2 NS and commercial RuO_2 was studied using the rotating disk electrode (RDE) technique in O_2-saturated 0.1 M perchloric acid solution. Before the electrochemical activity test, the catalysts were activiated and preoxidized through potential cycles between 0.1 V and 1.4 V *versus* RHE in N_2-saturated solution to obtain stable cyclic voltammetry curves and to avoid the disturbance of metal oxidation processes.[14] As shown in Figure 2a, the RuRh NS exhibits poor OER stability with fast activity fading for just a few cycles, implying that the metallic RuRh NS is not suitable for OER catalysis despite its high activity. In contrast, the RuRh@(RuRh)O_2 NS is much more stable than the RuRh NS (**Figure 2b**). The linear sweep voltammetry (LSV) curves of all catalysts normalized to the geometrical area of electrode with *iR* correction are shown in **Figure 2c**. It can be seen that the activity decreases in the order of RuRh NS > RuRh@(RuRh)O_2 NS>> commercial RuO_2, revealing that the RuRh NS exihibts the high OER activity whereas the RuRh@(RuRh)O_2 NS retains the high activity after the annealing process. The overpotentials of RuRh NS, RuRh@(RuRh)O_2 NS and commercial RuO_2 at 10 mA cm^{-2} are 213 mV, 245 mV and 314 mV (**Figure 2d**). The corresponding Tafel slopes (**Figure S9**) are 49.3 mV dec^{-1}, 51.2 mV dec^{-1} and 110.3 mV dec^{-1}, respectively, indicating the favorable reaction kinetics of RuRh NS and RuRh@(RuRh)O_2 NS. The OER current densities converted into Platinum Group Metal (PGM) mass-based activities (units of $A\,g_{PGM}^{-1}$) of the catalysts are shown in **Figure S10**. The mass activities of RuRh NS and RuRh@(RuRh)O_2 NS at the overpotential of 250 mV are 437.4 $A\,g_{PGM}^{-1}$ and 119.8 $A\,g_{PGM}^{-1}$, which are 16.6 and 4.6 times higher than the commercial RuO_2, respectively. Compared with the most state-of-the-art Ru-based or Ir-based electrocatalysts for OER, the RuRh@(RuRh)O_2 NS is of low overpotential and favorable reaction kinetics (**Table S1**).

It remains a critical issue of catalytic stability of the OER catalysts especially in acid electrolyte due to the corrosive conditions under which OER catalysts operate.[15] As mentioned above, the RuRh NS exhibits poor OER stability of fast fading for just a few cycles while the RuRh@(RuRh)O_2 NS are more stable than the RuRh NS. The rotating ring disk electrode (RRDE) method was used to clarify the fast fading of RuRh NS. In the RRDE experiment, employed in a "collection mode", the ring electrode is held at a constant potential

at which Ru cations dissolved from disk electrodes in the solution phase should deposit onto the ring electrode while simultaneously recording the OER on the central Ru disk electrode.[16] As shown in **Figure 3a**, the onset of Ru dissolution is accompanied by the onset of the OER, and the disk current of RuRh NS at 1.53 V is about 92 uA, 224 times higher than that of RuRh@(RuRh)O_2 NS, indicating that the RuRh@(RuRh)O_2 NS is much more stable than the metallic RuRh NS during OER process due to much lesser Ru dissolution, attributed to the oxidization of RuRh to low-index rutile structured RuO_2/RhO_2.[17] The RRDE results analysis (**Table S2**) further indicates that the contribution of the current corresponding to Ru dissolution relative to the total anodic current measured on the disk electrodes is only 0.049 % for RuRh@(RuRh)O_2 NS and 7.3 % for RuRh NS, implying that the Faradaic efficiency of the OER for RuRh@(RuRh)O_2 NS (approximately 99.9 %) is much higher than that for RuRh NS (92.7 %) (**Figure 3b**).

The stability was further evaluated by chronopotentiometry at constant current of 5 mA cm^{-2} (**Figure 3c**). The results indicate that the RuRh@(RuRh)O_2 NS is much more stable than RuRh NS and commercial RuO_2. The amount of dissolved Ru in the electrolyte during OER are mesured by coupled plasma mass spectrometry (ICP-MS), and the results are shown in **Table S3**. The Ru dissolution rate of RuRh NS 4.0 ng cm^{-2} s^{-1}, 66.7 times higher than that of RuRh@(RuRh)O_2 NS (0.060 ng cm^{-2} s^{-1}), indicating that the shell structure of RuO_2/RhO_2 can protect the core of metallic RuRh NS from dissolving during the OER process, which is in accordance with the RRDE results. Hence, the RuRh@(RuRh)O_2 NS exhibts the enhanced OER catalytic stability compared with that of the RuRh NS.

The OER performance of RuRh@(RuRh)O_2 NS was also investigated in O_2-saturated 1 M KOH as well (**Figure S11**). The overpotential of RuRh@(RuRh)O_2 NS and commercial RuO_2 at 10 mA cm^{-2} are 304 mV and 362 mV, and the corresponding Tafel slope are 80.9 mV dec^{-1} and 165.1 mV dec^{-1}, respectively. Besides, RuRh@(RuRh)O_2 NS shows higher mass activities compared with the commercial RuO_2. The aboved results reveal that the RuRh@(RuRh)O_2 NS exhibits better OER acitivity in alkaline media as well compared with the commercial RuO_2.

We investigate the OER electrocatalysis in the core@shell RuRh@(RuRh)O_2 based on the constructed model through DFT calculations (**Figure 4a**). The surface oxidation layer evidentially becomes more electron-rich in RuRh@(RuRh)O_2, which supports the enhanced electron transfer capability (**Figure 4b**). In RuRh@(RuRh)O_2, the projected partial density of states (PDOS) shows

that the modulation of Ru-4d bands, in which the wide covering bands become concentrated with upshift of the d-band center. More importantly, the high electroactivity near the RuRh/RuO_2 interface supports that the close oxide/hydroxide next to the metal substrate is active for OER especially at low overpotential.[18] The evident alleviation of the e_g-t_{2g} gap on the electrocatalyst surface also demonstrates a smaller energy barrier for electron depletion, which is critical for actualizing efficient OER in the acid and alkaline environment (**Figure 4c**). The site-dependent PDOS of O-2p bands displays the crossover of Fermi level (E_F), indicating a high electron transfer capability to facilitate the interaction between electrocatalyst and the adsorbates (**Figure 4d**). Moreover, the free H_2O displays the dominant peak at E_V-2.5 eV, which highly matches with the Rh-4d bands. Similar well overlapping between the intermediates *s,p* bands, and the surface RhRu are also noted. This confirms the key role of Rh in facilitating the initial adsorption of H_2O and OH in acidic and alkaline media (**Figure 4e**). Further, we analyze the electronic structures in details regarding the band offset and the e_g-t_{2g} gap. From the core RuRh towards the surface RuO_2 layer, we observe the upshifting of Ru 4d-bands from E_V-2.2 eV to E_V-1.3 eV. This result supports the substantially enhanced electroactivity due to the formation of the surface oxidation layer (**Figure 4f**). Beyond the band offset, the obvious shrink of the gap between the e_g-t_{2g} occurs in the surface oxidation layer. The energy barrier evidentially decreases nearly half magnitude from the core RuRh of 2.9 eV to 1.4 eV in the shell RuO_2 surface (**Figure 4g**). Similarly, the p-bands of O in the surface oxidation layer shows the downshifting from the surface RuO_2 to the RuRh/RuO_2 interface. Thus, the efficient electron transfer from catalyst towards adsorbates is achieved by the surface oxidation layer (**Figure 4h**). Meanwhile, the high electrical conductivity of the core RuRh paves a good way of electron transfer from the electron-rich core towards the electroactive shell RuO_2 surface. The collaborated contribution of RuRh and RuO_2 results in the superior OER performance in in acidic and alkaline media.

We also unveil the energetic pathway to illustrate the physicochemical reaction trend of the core@shell RuRh@(RuRh)O_2 in both acidic and alkaline OER. For the acidic OER, the reaction of [$*OH+H_2O+H^+ \rightarrow *O+ H_2O+2H^+$] requires the highest energy cost of 1.45 eV under U = 0 V, indicating the corresponding overpotential of 0.22 V to achieve the complete downhill trend of OER process, which is highly consistent with the experimental results (**Figure 4i**). Meanwhile, we observe the rate-determining step as the reaction of [$*OH+ 3OH^- \rightarrow *O+ 2OH^- + H_2O$] with an energy barrier of 1.52 eV in the alkaline OER. The final formation of O_2 exhibits a similar barrier height. The corresponding overpotential of 0.29 V for alkaline OER is in a good agreement with the 304 mV overpotential from experiments (**Figure 4j**). There, the highly electroactive shell oxidation layer

significantly boosts up the electron transfer capability to actualize superior OER in acidic and alkaline media.

Conclusions

In summary, this work presents a rational design of ultrathin RuRh@(RuRh)O_2 core@shell nanosheets as highly stable and active OER electrocatalysts. The 2D mophology of ultrathin RuRh@(RuRh)O_2 core/shell nanosheets with high degree of abundant surface atoms serving as active sites guarantee the high OER activity and the shell structure of RuO_2/RhO_2 oxides could lower the fast Ru dissolution of metallic RuRh NS during OER process, certificated by rotating ring disk electrode (RRDE) measurements for simultaneously recording the dissolution of Ru on the ring electrode or the *ex-situ* measurement of Ru dissolution using the galvanostatic method. Therefore, the ultrathin RuRh@(RuRh)O_2 core@shell nanosheets exhibit much better OER stability than the metallic RuRh NS. DFT calculations unravel the superior OER performance based on the electro-activation by the surface oxidation layer. The core RuRh preserve the high electrical conductivity for electron transfer to the surface. The shell RuO_2 layer further pumps the electrons towards the adsorbates to efficiently facilitate the consecutive reactions in OER. The enhancement of the OER is guaranteed based on the synergistic contribution by the RuRh core and oxidation layer shell. The present work provides a new vision for tuning the ultrathin 2D heterostructures to balance the OER activity and stability.

Supporting Information

Supporting Information is available from the Wiley Online Library or from the author.

Acknowledgements

This work was financially supported by Beijing Natural Science Foundation (No. JQ18005), the "XPLORER PRIZE" (Tencent), the National Natural Science Foundation of China (No. 51671003), National Key R&D Program of China (No. 2016YFB0100201), BIC-ESAT project, the China Postdoctoral Science Foundation (No. 2017M610022) and Young Thousand Talented Program.

Conflict of Interest

The authors declare no competing interests.

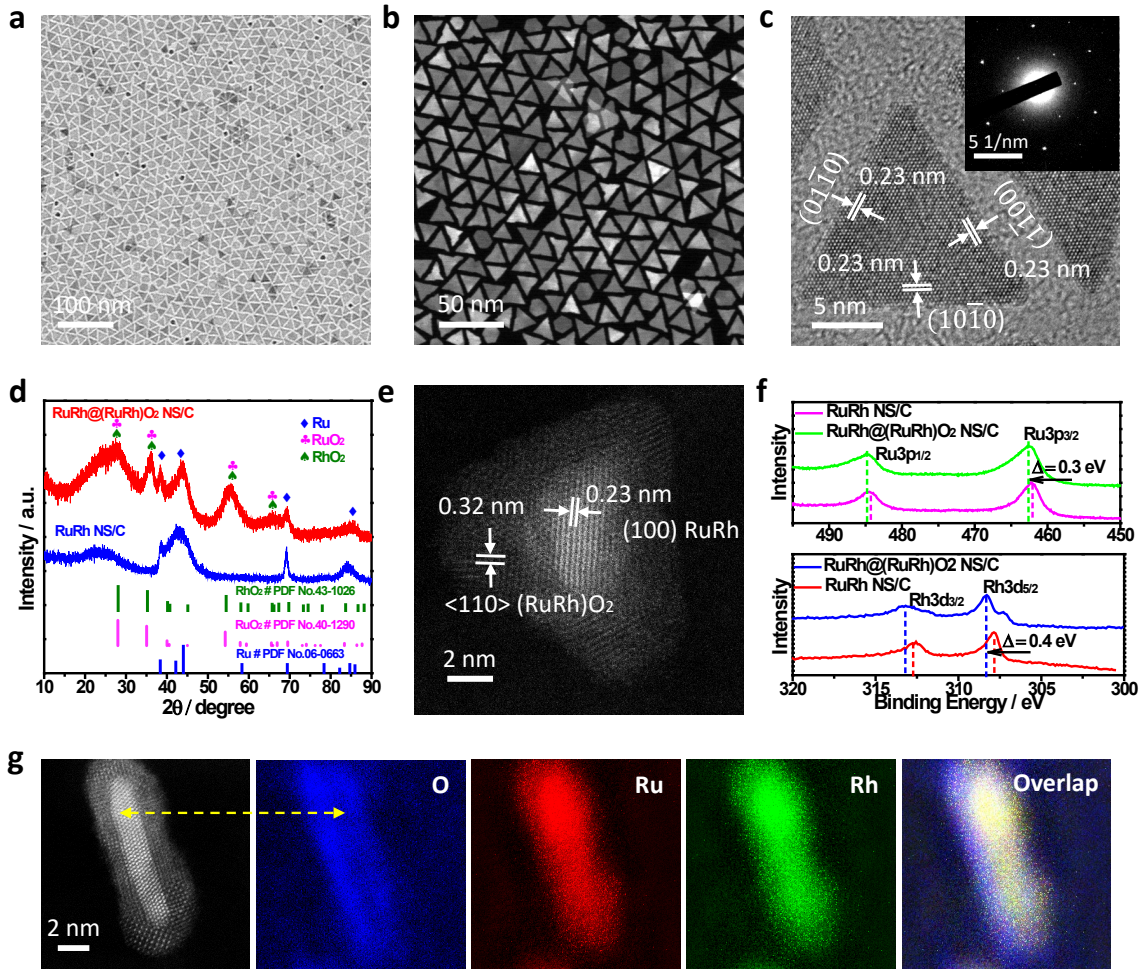

Figure 1. Morphology and structure characterization of ultrathin RuRh NS and RuRh@(RuRh)O_2 NS. Representative (a) TEM image and (b) HAADF-STEM image of ultrathin RuRh NS. (c) HRTEM TEM image of ultrathin RuRh NS (The *inset* shows the related SAED image). (d) PXRD patterns and (e) HAADF-STEM image of the RuRh@(RuRh)O_2 NS. (f) XPS analysis of Rh 3d and Ru 3p spectra. (g) STEM-EDX elemental mapping of the RuRh@(RuRh)O_2 NS.

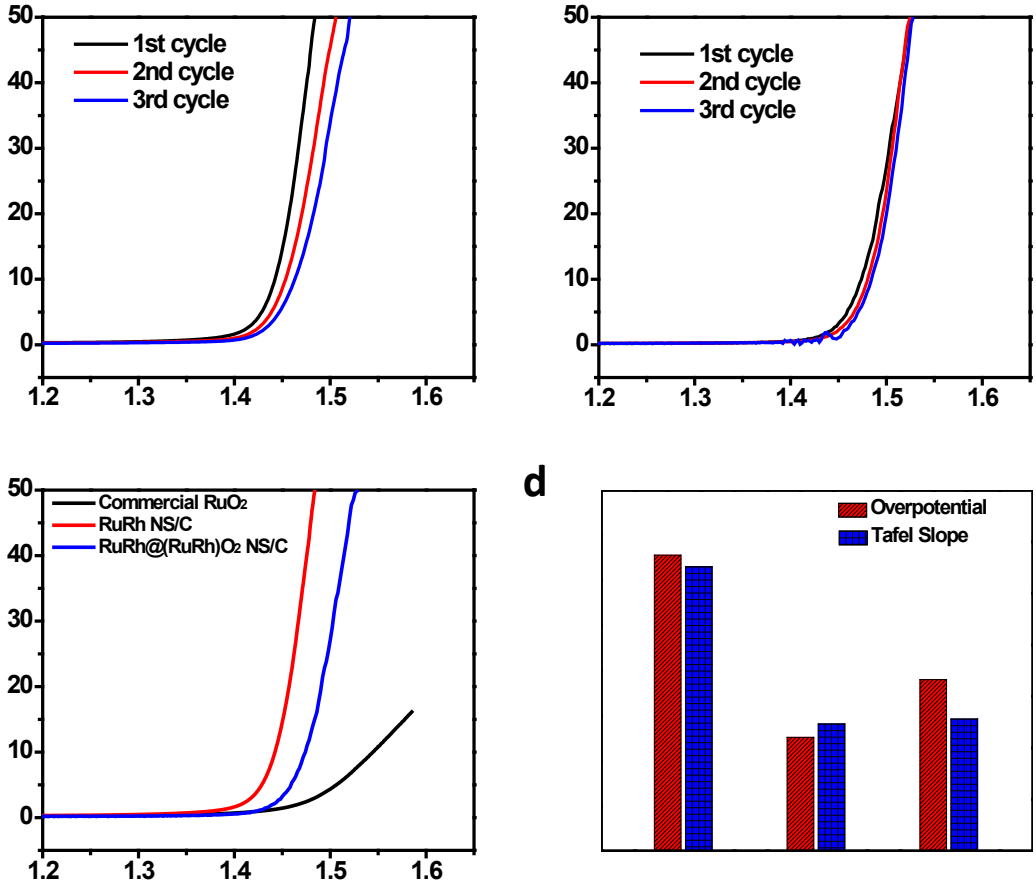

Figure 2. Electrochemical performance of RuO_2, RuRh NS and RuRh@(RuRh)O_2 NS in O_2-saturated 0.1 M $HClO_4$. LSV curves of the (a) the RuRh NS and (b) RuRh@(RuRh)O_2 NS in 0.1 M $HClO_4$ at 1600 rpm with scan rate 10 mV s^{-1} at the first few cycles. (c) LSV curves of the first cycle, (d) overpotentials at 10 mA cm^{-2} and Tafel slopes of RuO_2, RuRh NS and RuRh@(RuRh)O_2.

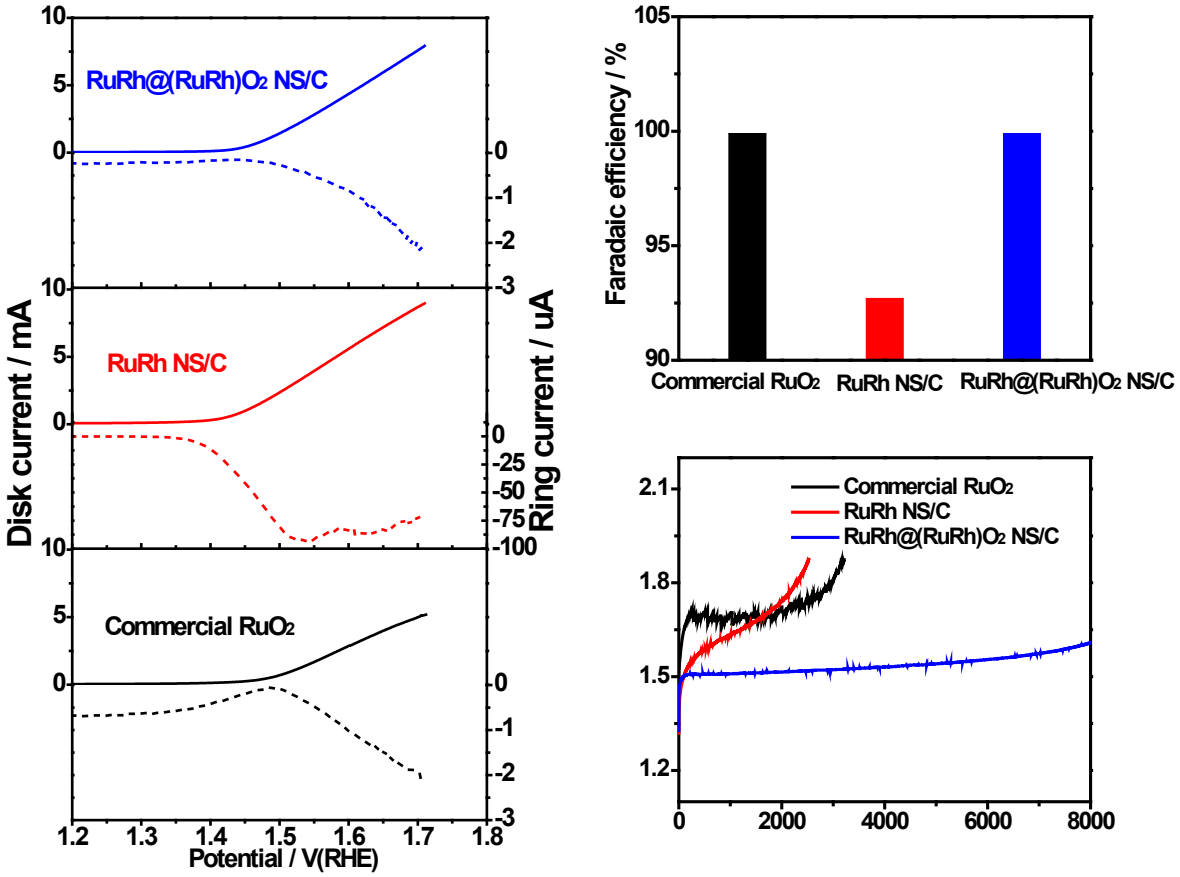

Figure 3. OER stability of Commercial RuO_2, RuRh NS and RuRh@(RuRh)O_2 NS. (a) Rotating ring disk electrode (RRDE) measurements in O_2-saturated 0.1 M $HClO_4$ for simultaneously recording the OER on the central disk electrode and the dissolution of Ru on the ring electrode (E_{ring} = 0.9 V) and (b) Faradaic efficiency of the OER at 1.53 V. (c) Chronopotentiometry tests of the catalysts in 0.1 M $HClO_4$ at 5 mA cm^{-2}.

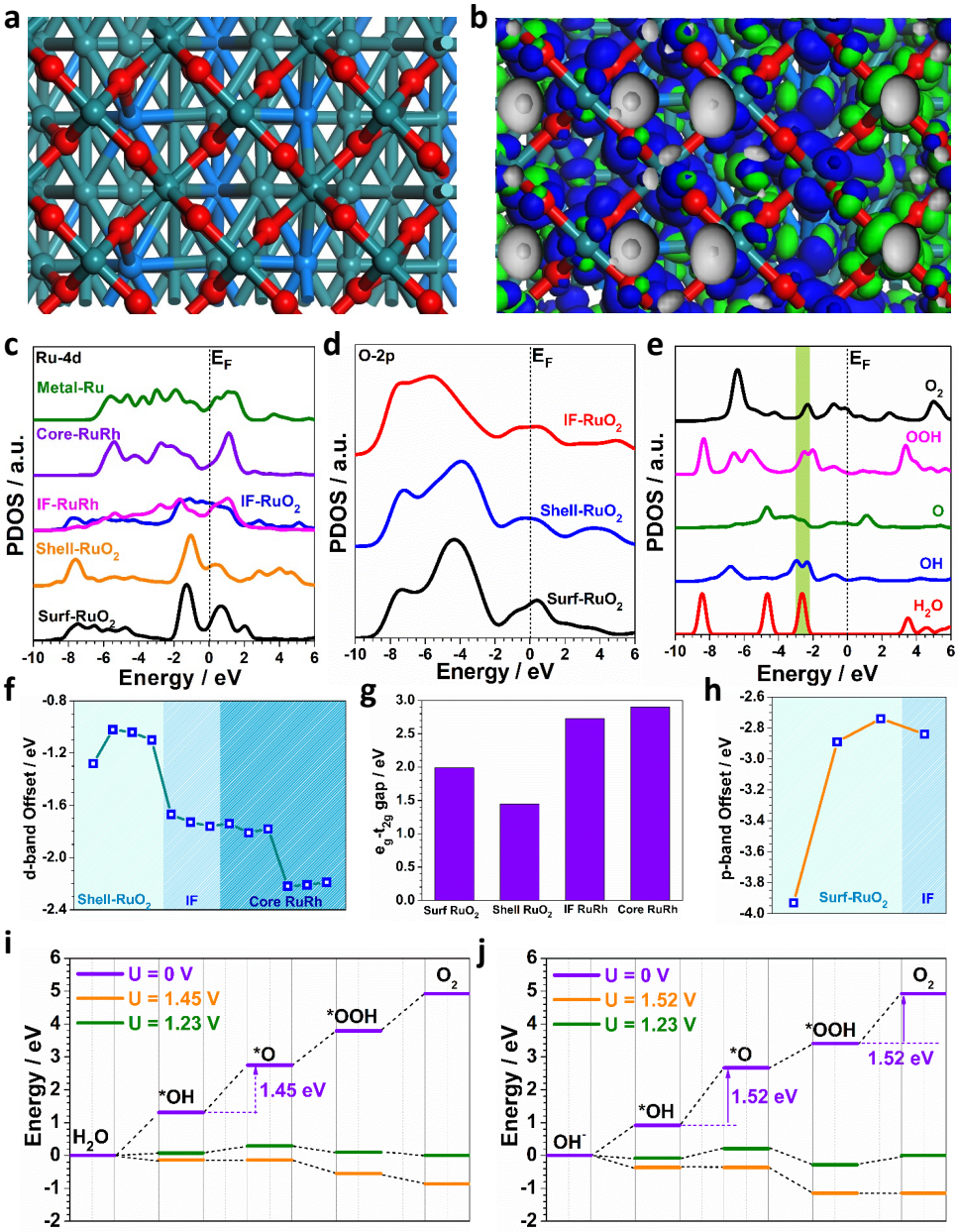

Figure 4 Electronic properties, structure configurations and energetic pathway of RuRh@(RuRh)O_2 for OER. (a) Top view of the core-shell RuRh@(RuRh)O_2 structure. Blue balls = Rh; Cyan balls = Ru; Red balls = O. (b) The real spatial contour plots for bonding and anti-bonding orbitals near E_F of RuRh@(RuRh)O_2. (c) The site-dependent PDOSs comparison of Ru-4d and Rh-4d in RuRh@(RuRh)O_2. (d) The site-dependent PDOS comparison of O-2p in RuRh@(RuRh)O_2. (e) The PDOS of key intermediates of OER. (f) The d-band offset of Ru-4d in RuRh@(RuRh)O_2. (g) The site-dependent e_g-t_{2g} gap in RuRh@(RuRh)O_2. (h) The p-band offset of Ru-4d in RuRh@(RuRh)O_2. (i) Energetic pathway of OER under the acidic condition. (j) Energetic pathway of OER under the alkaline condition.

References

[1] a) A. Grimaud, A. Demortière, M. Saubanère, W. Dachraoui, M. Duchamp, M.-L. Doublet, J.-M. J. N. E. Tarascon, **2017**, 2, 16189; b) H. N. Nong, T. Reier, H.-S. Oh, M. Gliech, P. Paciok, T. H. T. Vu, D. Teschner, M. Heggen, V. Petkov, R. Schlögl, *Nature Catalysis* **2018**, 1, 841; c) L. C. Seitz, C. F. Dickens, K. Nishio, Y. Hikita, J. Montoya, A. Doyle, C. Kirk, A. Vojvodic, H. Y. Hwang, J. K. Norskov, *Science* **2016**, 353, 1011.

[2] a) J. Shan, C. Guo, Y. Zhu, S. Chen, L. Song, M. Jaroniec, Y. Zheng, S.-Z. J. C. Qiao, **2019**, 5, 445; b) J. Feng, F. Lv, W. Zhang, P. Li, K. Wang, C. Yang, B. Wang, Y. Yang, J. Zhou, F. Lin, *Advanced Materials* **2017**, 29, 1703798; c) T. Reier, H. N. Nong, D. Teschner, R. Schlögl, P. Strasser, *Advanced Energy Materials* **2017**, 7, 1601275.

[3] C. Spoeri, J. T. H. Kwan, A. Bonakdarpour, D. P. Wilkinson, P. J. A. C. I. E. Strasser, **2017**, 56, 5994.

[4] J. Creus, J. De Tovar, N. Romero, J. García-Antón, K. Philippot, R. Bofill, X. J. C. Sala, **2019**.

[5] R. Forgie, G. Bugosh, K. Neyerlin, Z. Liu, P. J. E. Strasser, S.-S. Letters, **2010**, 13, B36.

[6] a) S. Cherevko, A. R. Zeradjanin, A. A. Topalov, N. Kulyk, I. Katsounaros, K. J. Mayrhofer, *ChemCatChem* **2014**, 6, 2219; b) M. Schalenbach, O. Kasian, M. Ledendecker, F. D. Speck, A. M. Mingers, K. J. Mayrhofer, S. Cherevko, *Electrocatalysis* **2018**, 9, 153.

[7] S. Cherevko, S. Geiger, O. Kasian, N. Kulyk, J.-P. Grote, A. Savan, B. R. Shrestha, S. Merzlikin, B. Breitbach, A. Ludwig, *Catalysis Today* **2016**, 262, 170.

[8] L. Gloag, T. M. Benedetti, S. Cheong, C. E. Marjo, J. J. Gooding, R. D. Tilley, *Journal of the American Chemical Society* **2018**.

[9] A.-X. Yin, W.-C. Liu, J. Ke, W. Zhu, J. Gu, Y.-W. Zhang, C.-H. Yan, *Journal of the American Chemical Society* **2012**, 134, 20479.

[10] K.-P. Bohnen, R. Heid, O. de la Pena Seaman, B. Renker, P. Adelmann, H. Schober, *Physical Review B* **2007**, 75, 092301.

[11] R. Shannon, *Solid State Communications* **1968**, 6, 139.

[12] L. Bu, Q. Shao, Y. Pi, J. Yao, M. Luo, J. Lang, S. Hwang, H. Xin, B. Huang, J. Guo, *Chem* **2018**, 4, 359.

[13] D. J. Morgan, *Surface and Interface Analysis* **2015**, 47, 1072.

[14] F. Lv, J. Feng, K. Wang, Z. Dou, W. Zhang, J. Zhou, C. Yang, M. Luo, Y. Yang, Y. J. A. c. s. Li, **2018**, 4, 1244.

[15] a) B. Han, M. Risch, S. Belden, S. Lee, D. Bayer, E. Mutoro, Y. Shao-Horn, *Journal of The Electrochemical Society* **2018**, 165, F813; b) C. Wei, R. R. Rao, J. Peng, B. Huang, I. E. Stephens, M. Risch, Z. J. Xu, Y. J. A. M. Shao‐Horn, **2019**, 1806296.

[16] N. Danilovic, R. Subbaraman, K.-C. Chang, S. H. Chang, Y. J. Kang, J. Snyder, A. P. Paulikas, D. Strmcnik, Y.-T. Kim, D. Myers, *The journal of physical chemistry letters* **2014**, 5, 2474.

[17] Y. Lee, J. Suntivich, K. J. May, E. E. Perry, Y. Shao-Horn, *The journal of physical chemistry letters* **2012**, 3, 399.

[18] S. Zou, M. S. Burke, M. G. Kast, J. Fan, N. Danilovic, S. W. J. C. o. M. Boettcher, **2015**, 27, 8011.